Interdisciplinary Research in Medical Sciences Specialty
ISSN: 3062-4401
2026, Volume 6, Issue 1, Page No: 99-115

Available online at: www.galaxypub.co/page/journals

Galaxy Publication

Red Blood Cell Membrane-Derived NIR-II Biohybrid Nanovesicles Enable Synergistic Mild-Temperature Photothermal and Antibiofilm Therapy

Lukas Weber[1]*, Sophie Janssen[2], Jonas Richter[1], Elena Fischer[3]

[1]Department of Nanovesicles and Photothermal Therapy, Faculty of Medicine, University of Stuttgart, Stuttgart, Germany.
[2]Department of Biohybrid Systems and Antibiofilm Research, Faculty of Pharmaceutical Sciences, Eindhoven University of Technology, Eindhoven, Netherlands.
[3]Department of Mild-Temperature Photothermal Agents, Faculty of Medicine, University of Basel, Basel, Switzerland.

***E-mail** ✉ lukas.weber@uni-stuttgart.de

Received: 22 April 2026; **Revised:** 23 June 2026; **Accepted:** 27 June 2026

ABSTRACT

The development of antibiotic-resistant bacteria represents a major obstacle to the effective and timely management of bacterial infections, including acute bacterial skin and skin-structure infections (ABSSSI), particularly when biofilms are present. Bacterial biofilms exhibit inherent resistance to antibiotics and the host immune response, rendering biofilm-associated infections exceptionally challenging to eradicate. Consequently, the creation of novel antibacterial strategies that specifically target biofilms is of critical importance. Aggregation-induced emission luminogens exhibiting fluorescence in the second near-infrared window (NIR-II AIEgens), which can be activated by near-infrared laser irradiation to produce heat, provide a highly effective and targeted approach for photothermal therapy (PTT) in the treatment of deep-tissue bacterial infections. Nevertheless, biofilms hinder the penetration of photosensitizers into the infected site, often necessitating elevated drug concentrations and thereby increasing the potential risks associated with PTT. In this work, we engineered a biocompatible AIEgen-based biohybrid nanoformulation that integrates the NIR-II AIEgen BPBBT with antibiofilm α-amylase within a nanovesicle carrier derived from red blood cell (RBC) membranes, enabling a combined PTT and biofilm degradation strategy. The synergistic interaction of this formulation markedly improves both the photothermal performance of BPBBT and biofilm disruption relative to conventional monotherapies. This innovative combination therapy exhibited substantial efficacy in addressing severe Staphylococcus aureus biofilm-mediated infections both in vitro and in vivo, offering a promising alternative to conventional antibiotic treatments.

Keywords: Aggregation-induced emission, Anti-biofilm materials, Biofilm, Nanovesicle, Photothermal therapy

How to Cite This Article: Weber L, Janssen S, Richter J, Fischer E. Red Blood Cell Membrane-Derived NIR-II Biohybrid Nanovesicles Enable Synergistic Mild-Temperature Photothermal and Antibiofilm Therapy. Interdiscip Res Med Sci Spec. 2026;6(1):99-115. https://doi.org/10.51847/GSzIPCF9r3

Introduction

Acute bacterial skin and skin-structure infections (ABSSSI) are frequently encountered in clinical settings and are typically managed with antibiotic therapy [1, 2]. However, the overuse of antibiotics has contributed to the emergence of multidrug-resistant bacterial strains in nearly 80% of cases, which are unresponsive to standard antibiotic treatments [3, 4]. Furthermore, bacterial biofilms, composed of diverse extracellular polymeric substances (EPS), severely restrict antibiotic penetration and amplify the resistance and tolerance of pathogenic bacteria [5-7]. Within biofilms, bacteria can exchange drug-resistance plasmids, decreasing their susceptibility to antibiotics by as much as 1000-fold [7, 8]. As a result, biofilm-associated infections are particularly recalcitrant to treatment and frequently recur following the discontinuation of antimicrobial therapy [9]. Although several non-antibiotic approaches for biofilm management exist—such as chitosan [10], antimicrobial peptides and their

biomimetic polymers [11], graphene oxide [12], and biofilm-degrading enzymes [5]—their clinical utility is constrained by issues including poor stability, brief systemic circulation times, and potential biological toxicity. Therefore, the development of innovative antibiofilm therapies remains essential.

Photothermal therapy (PTT) has emerged as a promising therapeutic modality, attracting considerable interest for applications in oncology [13], neurodegenerative disorders [14], and infectious diseases [15]. PTT induces localized thermal damage through the conversion of light energy into heat by photothermal agents (PTAs), enabling the selective elimination of target cells [16] while demonstrating broad-spectrum antibacterial activity without promoting bacterial resistance [17]. Moreover, elevated temperatures can dismantle established biofilms [18] and enhance tissue oxygenation via improved blood circulation, thereby accelerating wound healing [19]. Among various PTAs, NIR-II emissive aggregation-induced emission luminogens (NIR-II AIEgens) with near-infrared absorption (longer than 700 nm) and minimal toxicity have garnered increasing attention owing to their dynamic intramolecular motion and superior photothermal conversion efficiency. Additionally, their fluorescence emission within the NIR-II biological window (1000–1700 nm) experiences reduced absorption and scattering by biological tissues, resulting in negligible phototoxicity and greater biological tolerance compared with shorter-wavelength irradiation [20-25]. These attributes position NIR-II AIEgens as excellent candidates for the PTT of deep-seated lesions, with significant potential in antibacterial applications [26, 27]. Nonetheless, the therapeutic efficacy of PTT is frequently compromised by the limited diffusion of PTAs due to the protective EPS matrix of bacterial biofilms [5-7, 28]. Furthermore, the elevated temperatures generated by conventional PTT may induce irreversible harm to adjacent healthy tissues [29, 30].

Combination therapy represents a viable strategy to lower the required PTA dosage and laser intensity, thereby achieving milder hyperthermia while maintaining or enhancing PTT efficiency and minimizing collateral thermal damage to surrounding normal tissues [31, 32]. Earlier research has demonstrated that α-amylase effectively degrades bacterial EPS, thereby disrupting biofilm integrity [5]. Notably, α-amylase retains robust enzymatic activity across a broad temperature range (10°C–70°C) and displays peak performance near 50°C [33]. This property renders it particularly suitable for integration with moderate-temperature PTT. Nanocarriers derived from cell membranes offer an advantageous platform for combination therapies, enhancing biocompatibility and mitigating drug-related toxicity [34, 35] while avoiding the formation of biocorona that typically occurs with conventional nanoparticles upon contact with blood components [35]. By retaining the native biological functions of their source cell membranes, these carriers can evade immune recognition, extend blood circulation time, and improve site-specific targeting [36]. Cell membrane sources include tumor cells, immune cells, red blood cells, platelets, and others [37]. Red blood cells are especially advantageous, as they lack nuclei and organelles, facilitating straightforward processing and removal of intracellular contents. The resulting emptied RBCs can serve as coatings for nanoparticles or be reassembled into nanovesicles [38], yielding biomimetic nanovesicles.

In the present study, we describe the development of NIR-II emissive biohybrid nanovesicles incorporating NIR-II AIEgens and α-amylase into multi-compartment nanocargoes derived from cell membranes, formulated as a biocompatible and refreshed mild-temperature photothermal antibiofilm platform. As illustrated in Scheme 1, BPBBT (a representative NIR-II emissive AIEgen with near-infrared absorption) [39-41] was integrated into the outer lipid bilayer compartment of nanovesicles prepared from natural red blood cell (RBC) membranes. Concurrently, α-amylase was encapsulated within the inner aqueous core compartment of the nanovesicles (designated nano-MBA) through electroporation. Upon irradiation with an 808 nm laser, the nanovesicles generate localized photothermal heating and trigger the release of α-amylase. The resulting temperature elevation optimizes the enzymatic activity of α-amylase, thereby potentiating biofilm degradation. In turn, the enzymatic hydrolysis of the biofilm matrix facilitates deeper penetration of BPBBT into the infected region, amplifying the overall photothermal therapeutic effect. This novel formulation establishes an effective antibiofilm strategy for ABSSSI associated with Staphylococcus aureus (S. aureus or S.A.) biofilms through mild-temperature photothermal ablation.

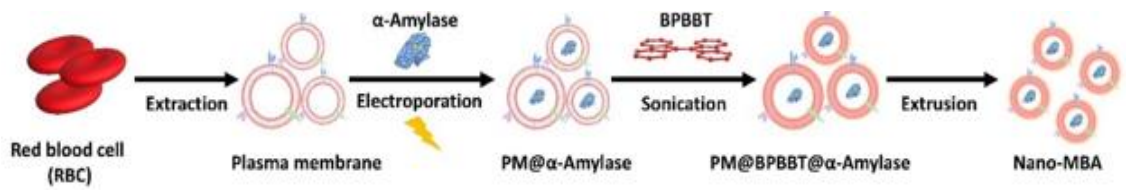

a)

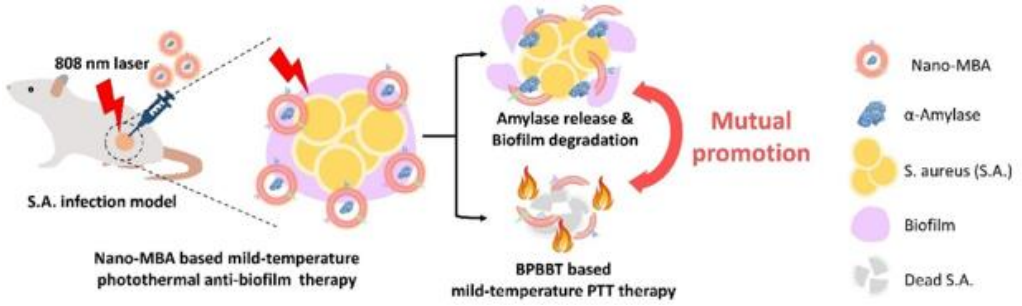

b)

Scheme 1. Design, fabrication, and operational mechanism of nano-MBA.

(a) Fabrication workflow of nano-MBA. (b) Mechanism of the combined therapy involving amylase-mediated biofilm degradation and enhanced PTT.

Materials and Methods

BPBBT (CAS 1070910-81-4), systematically named 4,8-Bis[4-(N,N-bis(4-octyloxyphenyl)amino)phenyl]benzo[1,2-c:4,5-c′]bis(thiadiazole)[1,2,5], was purchased from Wuxi Seniormaterial Co., Ltd. (China). Red blood cells derived from mice were supplied by Shanghai EK-Bioscience Biotechnology Co., Ltd. (China). The reagents tetrahydrofuran (THF), acetic acid, α-amylase, glucose, tryptic soy broth (TSB) culture medium, and sodium citrate were obtained from Sigma-Aldrich (USA). Cell culture components including Dulbecco's modified Eagle's medium (DMEM), fetal bovine serum (FBS), penicillin-streptomycin (P/S), and phosphate-buffered saline (PBS) were acquired from Gibco (USA). A 2.5% glutaraldehyde fixative solution was sourced from Sbjbio (China). The human embryonic kidney 293T cell line (CRL-3216) and Staphylococcus aureus strain (ATCC 25923) were obtained from the American Type Culture Collection. Additional biochemical reagents—BCA Protein Assay Kits, Super-Enhanced Cell Counting Kit-8, and crystal violet staining solution—were provided by Beyotime Biotechnology (China). LIVE/DEAD™ BacLight™ Bacterial Viability Kits were purchased from Thermo Fisher Scientific (USA). Ultrapure water for all preparations was produced using a Direct-Q® 5 UV Remote Water Purification System (Merck, USA).

General measurements

Absorption spectra in the ultraviolet–visible–near-infrared range were measured with a Lambda 25 spectrophotometer manufactured by PerkinElmer (USA). Fluorescence spectra were collected on an F900 spectrofluorometer from Edinburgh Instruments (UK). Morphological characterization by transmission electron microscopy (TEM) was conducted on a Tecnai G2 Spirit TWIN microscope operating at 120 kV (FEI, USA). Surface topography was examined using scanning electron microscopy (SEM) on an S4800 instrument (Hitachi, Japan). Hydrodynamic size and zeta potential values were determined via dynamic light scattering with a Zetasizer Nano ZS analyzer (Malvern Panalytical, UK). Real-time temperature changes in the samples were tracked employing a T630sc infrared camera (FLIR, USA). Near-infrared irradiation was delivered by a fiber-coupled 808 nm laser device (CNI, China).

Plasma membrane extraction

Red blood cells from mice were first pelleted by centrifugation at 1500 rpm for 5 min at 4 °C and subsequently washed twice with 1× PBS. Hypotonic lysis was induced by suspending the cells in 0.25× PBS, with the suspension kept on ice for 5 min. Following lysis, centrifugation at 13 500 rpm for 5 min at 4 °C was performed to collect the membrane fractions, which were then subjected to two additional washes with cold 1× PBS. The obtained plasma membrane vesicles were resuspended in ultrapure water or PBS and maintained at 4 °C until required. Quantification of the membrane material relied on protein content assessment using BCA Protein Assay Kits.

Preparation of PM@BPBBT co-assemblies

A volume of 25 μL of BPBBT dissolved in THF at 4 mg/mL was introduced with stirring into 500 μL aliquots of plasma membrane suspensions adjusted to concentrations of 100 μg/mL, 200 μg/mL, 300 μg/mL, 400 μg/mL, or

600 μg/mL. This step generated co-assemblies with PM to BPBBT mass ratios of 0.5/1, 1/1, 1.5/1, 2/1, and 3/1. Organic solvent removal was achieved through 10 min of sonication, after which the mixtures were incubated at 37 °C for 60 min to facilitate self-assembly. Optical absorption, fluorescence emission, and photothermal heating profiles of these co-assemblies were systematically evaluated across the different mass ratios under 808 nm laser exposure at power densities ranging from 0.4 to 2.0 W/cm² (specifically 0.4, 0.8, 1.2, 1.6, and 2.0 W/cm²). Performance was compared against BPBBT in pure THF solution or in a 10:90 THF–water mixture. The most suitable mass ratio was selected according to the collective results from these characterizations.

Preparation of nano-MBA, nano-MA, nano-MB, and nano-RBM

Plasma membrane stock was diluted to a working concentration of 1 mg/mL. Separately, a 10 mg/mL α-amylase solution was prepared by dissolving 10 mg of the enzyme in 1 mL of ultrapure water. A total of 150 μL of this α-amylase solution and 100 μL of the diluted plasma membrane were mixed with 250 μL of ultrapure water, yielding final concentrations of 3000 μg/mL α-amylase and 200 μg/mL membrane material. The combined suspension was electroporated at 400 V and 150 μF using a Bio-Rad system to promote enzyme encapsulation, followed by a 45 min recovery period at 37 °C. Subsequently, 25 μL of 4 mg/mL BPBBT in THF was added under stirring, and the THF was eliminated by 10 min sonication to reach a final BPBBT concentration of 200 μg/mL. The resulting dispersion was incubated at 37 °C for 60 min and then extruded through a 0.22 μm membrane filter to yield nano-MBA nanoparticles. Analogous procedures, with compositional adjustments achieved by substituting omitted components with ultrapure water, were followed to prepare nano-MA, nano-MB, and nano-RBM.

Bacteria and biofilm cultivation

A fresh colony of S. aureus was picked from an LB agar plate and transferred into 5 mL of TSB citrate medium (TSBC), which consisted of standard TSB supplemented with 0.6% yeast extract, 0.8% glucose, and 0.2% sodium citrate. Overnight culture was carried out at 37 °C with shaking at 220 rpm to obtain bacteria in logarithmic growth phase. Optical density at 600 nm OD600 = 0.1 was measured using a Synergy 4 microplate reader (BioTek, USA) to determine bacterial concentration, where an OD600 of 0.1 equated to roughly 1×10^7 CFU/mL. Mature biofilms were grown by diluting the bacterial suspension to 1×10^6 CFU/mL in TSBC medium, dispensing 100 μL into each well of 96-well U-bottom plates, and incubating statically at 37 °C for 36 h. For confocal imaging experiments, biofilms were cultivated in 8-well chamber slides under otherwise identical conditions to those used in the 96-well plate format.

In vitro antibacterial evaluation

Once biofilms had fully matured in the 96-well plates, the overlying culture medium was discarded. Each well then received 100 μL of one of the following preparations: nano-MBA, nano-MA, nano-MB, nano-RBM, or PBS control (with RBC membrane at 200 μg/mL, BPBBT at 200 μg/mL, and α-amylase at 3 mg/mL). Incubation continued at 37°C for an additional 2 h. To investigate the impact of photothermal treatment and combined therapeutic strategies against biofilms, six replicate wells per nanovesicle formulation or PBS were subjected to 808 nm laser irradiation at 0.8 W/cm² for 10 min. Parallel sets of six wells for each condition remained unirradiated to enable direct comparison. Antibacterial efficacy was determined for every experimental group through multiple complementary approaches, including enumeration of viable bacteria, assessment of cellular morphology, measurement of total biofilm mass, and fluorescence-based live/dead cell visualization.

Viable bacterial counting assay

Following the application of the various treatment regimens to biofilms cultured in 96-well plates, the TSBC supernatant containing planktonic S. aureus was collected from each well and serially diluted (10×, 100×, 1000×, and 10 000×). These dilutions were spread onto LB agar plates and incubated at 37°C for 18 h. Colony-forming units were subsequently quantified using a Scan 300 colony counter (Interscience, France).

Bacterial morphology observation

After the biofilms in 96-well plates underwent the specified treatments, planktonic S. aureus cells from the TSBC supernatant were fixed with 2.5% glutaraldehyde for 30 min and allowed to adhere onto clean silicon wafers. Gradual dehydration was performed by sequential immersion in ethanol solutions of increasing concentration (30%, 50%, 70%, 80%, 90%, and 100%), with each step lasting 15 min, followed by complete drying overnight.

The prepared specimens were then sputter-coated with gold, and bacterial surface morphology was analyzed via scanning electron microscopy.

Biofilm biomass quantification

Upon completion of the different treatments applied to biofilms in 96-well plates, the supernatant TSBC medium was removed and replaced with 100 μL of 0.1% crystal violet solution per well for staining. After 15 min, the plates were rinsed gently three times with PBS and documented photographically. To quantify retained biofilm biomass, 200 μL of 30% acetic acid was added to each well to dissolve the crystal violet dye. A 100 μL portion of the resulting solution from every well was transferred to a new plate, and absorbance was recorded at 590 nm.

Live/dead bacterial staining and confocal imaging

After the assigned treatments of biofilms cultivated in 8-well chamber slides, the TSBC supernatant was aspirated. The remaining biofilms were incubated for 30 min with SYTO 9 and propidium iodide (components of the LIVE/DEAD™ BacLight™ Bacterial Viability Kits) to fluorescently label live and dead S. aureus cells, respectively. Subsequent visualization was performed using a TCS SP8 laser scanning confocal microscope (Leica, Germany).

Establishment of in vivo subcutaneous S. aureus biofilm infection mouse models

Forty-three female Balb/c mice aged 6–8 weeks were acquired from Vital River Laboratory Animal Technology Co. Ltd (China) to generate subcutaneous biofilm infection models on day −1, one day prior to initiating photothermal or combination therapies. All procedures involving animals received prior approval from the Animal Care and Use Committee of the Shenzhen Institutes of Advanced Technology, Chinese Academy of Sciences (SIAT-IACUC-210312-YYS-NMZX-ZPF-A1715-01) and were carried out under appropriate anesthesia. The bacterial inoculum was prepared from an overnight TSBC culture by performing two washes with cold PBS through centrifugation at 3000 g for 10 min at 4°C, followed by resuspension in cold PBS to achieve a density of 1×10^9 CFU/mL. This suspension was kept on ice until administration. Mice were first anesthetized in a dedicated chamber with 2%–2.5% isoflurane mixed with 2 L/min oxygen under standard atmospheric pressure. After induction, the hair over the right thigh was removed. Body weight was recorded for each animal, after which 50 μL of the S. aureus inoculum was injected subcutaneously [42]. Successful model establishment was verified by the appearance of a subcutaneous abscess within 24 h after injection. At this 24 h time point, all mice were re-weighed, and abscess dimensions were measured with a caliper to obtain length (L) and width (W). Abscess area was calculated using the formula $A = \pi(L/2) \times W/2$.

In vivo NIR-II fluorescence imaging

Twenty-four hours post-inoculation, three S. aureus biofilm infection models displaying comparable body weights and abscess sizes underwent initial imaging on a NIR-II fluorescence system equipped with a 1000–1700 nm bandpass filter to capture endogenous background signals. Each model then received a local injection of 50 μL nano-MBA formulation (RBC membrane at 200 μg/mL, BPBBT at 200 μg/mL, and α-amylase at 3 mg/mL) into the infected region. Fluorescence images in the NIR-II window were subsequently obtained at multiple time intervals: 0, 1, 2, 4, 8, 12, and 24 h after nanovesicle delivery. The 0 h image was acquired right after injection, within approximately one minute. Upon completion of the imaging protocol, the mice were euthanized, after which their primary organs (heart, liver, spleen, lungs, and kidneys) and the infected tissue samples were excised for ex vivo fluorescence analysis.

In vivo combination therapy

At the 24 h mark after inoculation, the remaining 40 mice bearing subcutaneous S. aureus biofilm infections were randomly distributed into eight balanced groups based on body weight and abscess dimensions. Local administration of nano-MBA, nano-MA, nano-MB, or nano-RBM (each containing RBC membrane at 200 μg/mL, BPBBT at 200 μg/mL, and α-amylase at 3 mg/mL) was performed at the infection site. Two independent groups were assigned to each nanovesicle type. Two hours following injection, one group per nanovesicle received NIR laser exposure consisting of 808 nm irradiation at 0.8 W/cm² for 10 min, while the parallel four groups served as non-irradiated controls.

Throughout the observation period, abscess dimensions and animal body weights were recorded every other day, accompanied by photographic documentation of the infection sites. Monitoring extended for 6 days after the therapeutic intervention (totaling 7 days from initial infection), at the conclusion of which the animals were euthanized and major organs (heart, liver, spleen, lungs, kidneys) plus infected tissues were harvested. Selected organs and two infected tissue specimens per group were rinsed in cold 1× PBS, then fixed using 4% paraformaldehyde at room temperature for a minimum of 24 h. These samples were embedded in paraffin, sectioned, and processed for H&E staining. Masson's staining was additionally conducted on all infected tissue sections. Mounted slides were examined under an optical microscope (Eclipse Ci, Nikon, Japan) and digitally scanned in full (Panoramic MIDI, 3DHISTECH, Hungary). The three remaining infected tissue samples from each group were rinsed twice with cold 1× PBS, mechanically disrupted using sieves, and resuspended in 1 mL of cold 1× PBS. Bacterial viability was quantified from these suspensions via the serial dilution plating protocol outlined previously.

Assessment of in vitro cytotoxicity

293T cells were plated at 5000 cells per well in 96-well plates (six wells per condition) using DMEM and permitted to attach overnight. On the subsequent day, the medium was discarded and cells were rinsed twice with PBS. One hundred microliters of fresh DMEM containing nano-MBA, nano-MA, nano-MB, or nano-RBM at BPBBT concentrations of 0, 20, 100, 150, 200, or 300 μg/mL was added to the respective wells. Following a 24 h incubation period at 37°C, the medium was removed and cells were washed with PBS prior to evaluation of viability with the Super-Enhanced Cell Counting Kit-8.

Assessment of in vivo toxicity

A separate set of forty-eight healthy female Balb/c mice (6–8 weeks of age) was randomly assigned to eight groups (n = 6 each), matched by body weight. These mice were given local injections in the right thigh region with nano-MBA, nano-MA, nano-MB, or nano-RBM (RBC membrane: 200 μg/mL, BPBBT: 200 μg/mL, α-amylase: 3 mg/mL), with two groups allocated per nanovesicle. Two hours post-administration, one subgroup for each nanovesicle underwent 808 nm laser irradiation at 0.8 W/cm² for 10 min, while the remaining four subgroups received no laser exposure.

Twenty-four hours after treatment, all animals were euthanized for collection of whole blood and major organs (heart, liver, spleen, lungs, and kidneys). Routine blood analysis was conducted on an automatic hematology analyzer (BC-2800 Vet, Shenzhen Mindray Animal Medical Technology, China). Serum was isolated by centrifugation, and key hepatic and renal function parameters—alanine aminotransferase (ALT), aspartate aminotransferase (AST), alkaline phosphatase (ALP), urea (UREA), and creatinine (CRE)—were measured using an automatic biochemistry analyzer (Chemray 800, Rayto Life and Analytical Sciences, China). Histopathological examination of the major organs was carried out on H&E-stained paraffin sections through conventional light microscopy (Eclipse Ci, Nikon, Japan) and comprehensive digital slide scanning (Panoramic MIDI, 3DHISTECH, Hungary).

Data analysis and statistical evaluation

Fluorescence images depicting live and dead bacteria were processed using LAS X (Leica), ImageJ (National Institutes of Health, USA), and Origin 2019b (OriginLab, USA) software. Relevant fluorescent labels were converted to pseudocolors for clearer presentation. Quantitative results for nanovesicle hydrodynamic diameter, zeta potential, in vivo fluorescence signals, cellular viability, body weight progression curves, hematology data, and serum biochemistry values were statistically analyzed in Origin 2019b and reported as mean ± SD ($n \geq 3$). Comparisons between groups were evaluated by two-sample t-test, with significance levels indicated as $^{*}P < 0.05$, $^{**}P < 0.01$, $^{***}P < 0.001$, $^{****}P < 0.0001$.

Results and Discussion

Characteristics of BPBBT

BPBBT is recognized as a donor–acceptor–donor (D–A–D) type AIEgen characterized by strong NIR absorption and NIR-II emission [39, 40]. Its photophysical behavior is highly dependent on solvent polarity and the degree of molecular aggregation. As presented in **Figure 1a**, BPBBT in tetrahydrofuran (THF) displayed a broad

absorption band extending from 500 to 1000 nm in the visible-to-near-infrared region, with the main absorption maximum located near 725 nm. In pure THF, the fluorescence intensity of BPBBT remained low **(Figure 1b)**, consistent with unrestricted intramolecular motion in this solvent [43]. However, progressive addition of water to THF (water fractions from 30% to 90%) led to a substantial rise in fluorescence emission. This enhancement occurs as the hydrophobic BPBBT molecules aggregate in the increasingly aqueous environment. A subsequent reduction in intensity at higher polarity levels was attributed to the twisted intramolecular charge transfer (TICT) mechanism [40, 43, 44]. Furthermore, when the water content surpassed 90%, the emission peak shifted from 1047 nm to 1008 nm **(Figure 1b)**, reflecting the transition from the TICT state to the aggregation-induced emission (AIE) state [43]. These findings are in complete agreement with earlier reports.

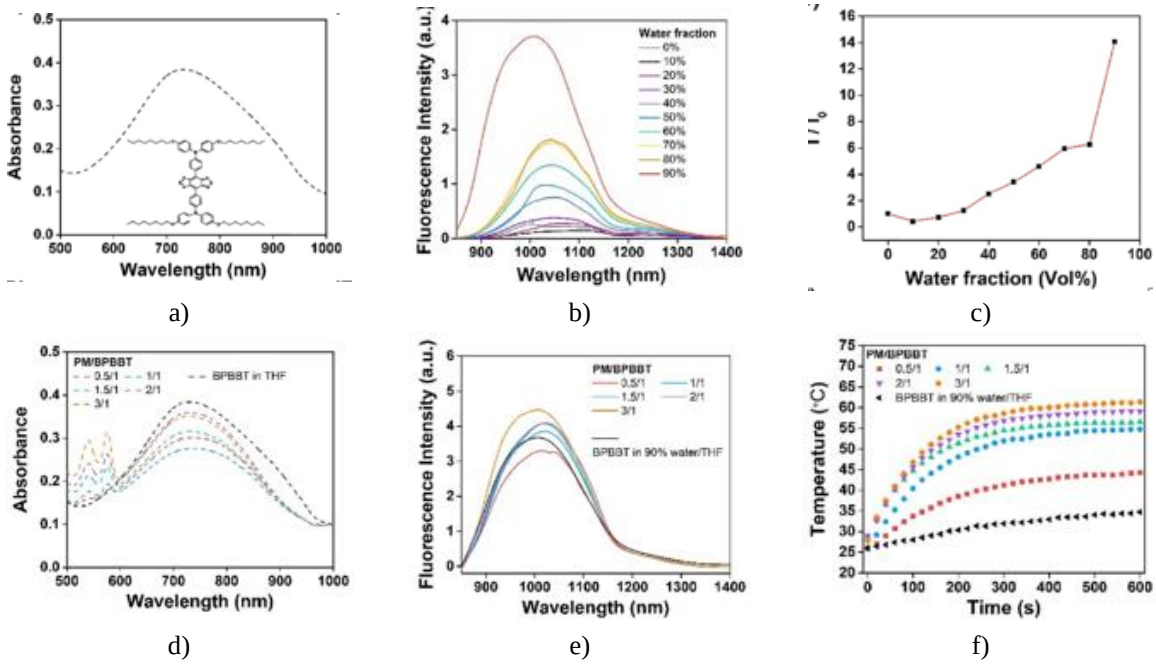

Figure 1. Characteristics of BPBBT.

(a) Chemical structure of BPBBT and its ultraviolet–visible (UV–vis) absorption spectra recorded in tetrahydrofuran (THF). (b) Fluorescence emission spectra of BPBBT in THF/water mixtures with water fractions ranging from 0% to 90% (excitation at 808 nm). (c) Relative fluorescence intensity (I/I0) of BPBBT as a function of water fraction in THF/water mixtures. I0 corresponds to the intensity in pure THF, while I represents the intensity in the mixed solvent. (d) UV–vis absorption spectra and (e) fluorescence emission spectra of PM nanoparticles loaded with BPBBT at varying mass ratios in aqueous dispersion. (f) Photothermal heating curves of aqueous dispersions of BPBBT-loaded PM nanoparticles with different mass ratios under 808 nm laser irradiation (0.8 W/cm², 10 min).

Preparation of BPBBT-loaded RBC membrane-derived nanovesicles

To facilitate an integrated therapeutic approach combining PTT with additional bioactive components, a tailored formulation strategy was implemented, as outlined in Scheme 1. RBC membranes were utilized due to their inherent biocompatibility and favorable safety profile originating from their natural source. For efficient incorporation of AIEgens such as BPBBT into the lipid bilayer of RBC membranes, BPBBT was initially dissolved in THF and subsequently mixed with the membrane suspension. This process relies on hydrophobic interactions between the AIEgen core and the lipid acyl chains [45]. Following THF removal by ultrasonication, spontaneous self-assembly occurred, yielding stable RBC membrane–BPBBT complexes. Given the tendency of hydrophobic compounds to embed within lipid bilayers from aqueous phases, BPBBT was anticipated to reside stably within the membrane structure [46]. The resulting hybrid is designated as PM@BPBBT.

Further optimization focused on enhancing NIR-II emission and photothermal conversion efficiency of PM@BPBBT under 808 nm laser exposure. UV–vis analysis confirmed successful BPBBT encapsulation across different PM/BPBBT mass ratios **(Figure 1d)**. At ratios between 0.5/1 and 3/1, the assembled nanoparticles generally exhibited superior NIR-II fluorescence **(Figure 1e)** and improved heat generation **(Figure 1f)** relative

to free BPBBT in THF/water (90/10, v/v), even with modestly reduced absorption **(Figure 1d)**. This outcome is noteworthy because AIEgens typically show diminished fluorescence and photothermal performance when formulated into conventional nanoparticles compared with their behavior in THF/water mixtures [40]. The current design therefore represents a significant advancement in preserving and augmenting AIEgen functionality for PTT applications.

Notably, an aqueous dispersion of PM@BPBBT at 200 μg/mL (prepared at a 1/1 PM/BPBBT ratio) achieved a temperature of 55°C after 10 min of 808 nm laser irradiation at 0.8 W/cm². This temperature is considered optimal for in vivo antibiofilm therapy, aligning with reports of effective biofilm disruption at around 50°C [47, 48]. Hence, the 1/1 mass ratio at a concentration of 200 μg/mL BPBBT was selected for further nanovesicle development. Photothermal performance was also shown to vary with nanoparticle concentration and laser power density, leading to the establishment of 200 μg/mL and 0.8 W/cm² as standard parameters.

Photostability assessments under these conditions revealed that PM@BPBBT retained 92.8% of its fluorescence intensity after 808 nm laser exposure at 0.8 W/cm², in contrast to only 42.7% retention by indocyanine green (ICG). Moreover, repeated heating–cooling cycles demonstrated no appreciable loss in maximum temperature (approximately 45°C) over five iterations, highlighting the robust photothermal stability of PM@BPBBT. Collectively, these data underscore the excellent fluorescence and thermal stability of the developed formulation, which supports its suitability for multiple NIR-II PTT sessions from a single dose.

Characterization of nano-RBM, nano-MA, nano-MB, and nano-MBA

Following the procedure outlined in Scheme 1, α-amylase was initially introduced into RBC membrane vesicles via electroporation to produce PM@α-amylase. BPBBT was then incorporated using the previously established optimal ratio, resulting in the formation of PM@BPBBT@α-amylase. Subsequent extrusion through 220 nm pore-size filters yielded the complete hybrid nanovesicles termed nano-MBA. For comparison, nanovesicles loaded solely with BPBBT (nano-MB) were generated by extruding PM@BPBBT. Similarly, enzyme-only nanovesicles (nano-MA) were prepared by processing PM@α-amylase through the same filtration step. Control blank RBC membrane nanovesicles (nano-RBM) were fabricated using the identical extrusion protocol.

As revealed by transmission electron microscopy, the nano-MBA, nano-MA, and nano-MB formulations displayed morphological profiles indistinguishable from those of the unloaded nano-RBM **(Figure 2a)**. This observation suggests that the fundamental vesicular framework originating from RBC membranes was preserved, and the inclusion of both α-amylase and BPBBT did not alter the overall configuration of these nanovesicles. Supporting data from dynamic light scattering and zeta potential measurements **(Figures 2b and 2c)** indicated close similarity in key physical attributes across all variants: nano-RBM (231.0 ± 5.597 nm, −11.5 ± 0.571 mV), nano-MA (207.1 ± 9.566 nm, −10.8 ± 0.697 mV), nano-MB (188.7 ± 8.103 nm, −10.5 ± 0.686 mV), and nano-MBA (202.6 ± 3.550 nm, −11.8 ± 0.748 mV). These results confirm that the drug-loading steps introduced negligible modifications to particle dimensions or surface charge characteristics of the RBC membrane-based nanovesicles.

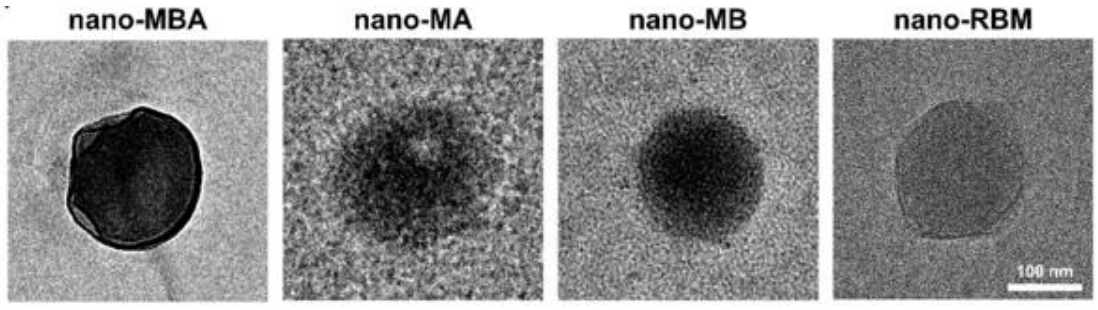

a)

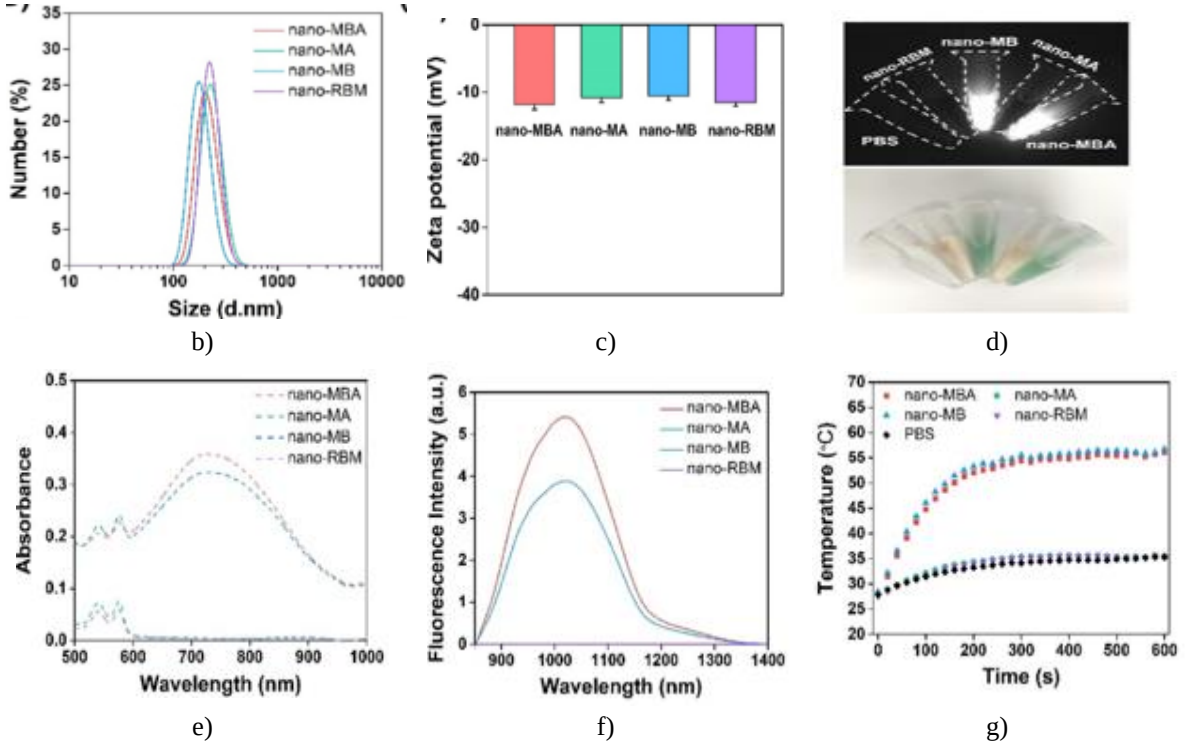

b) c) d)

e) f) g)

Figure 2. Physicochemical characterization of the fabricated nanovesicles.
(a) Transmission electron microscopy (TEM) images of nano-MBA (PM@BPBBT@α-amylase), nano-MA (PM@α-amylase), nano-MB (PM@BPBBT), and nano-RBM (blank RBC membrane nanovesicles). Scale bar: 100 nm. (b) Hydrodynamic size distributions and (c) zeta potential values of the different nanovesicles. (d) NIR-II fluorescence imaging with corresponding bright-field photographs. (e) Absorption spectra and (f) fluorescence emission spectra of the nanovesicles. (g) Photothermal heating curves of various nanovesicle suspensions exposed to 808 nm laser irradiation (0.8 W/cm²) for 10 min. Error bars represent mean ± s.d. (n = 3).

Assessment of the fluorescence behavior demonstrated that only the BPBBT-containing nano-MB and nano-MBA possessed the distinctive absorption profile of BPBBT, featuring a broad band from 500 to 1000 nm with a maximum near 725 nm of comparable strength **(Figure 2e)**. Under 808 nm excitation, these two formulations alone produced prominent emission spectra within the NIR-II range, peaking at approximately 970 nm with similar intensities **(Figure 2f)**. Such outcomes establish that α-amylase encapsulation exerts no adverse effect on the optical attributes of BPBBT in the nano-MBA construct. This conclusion was reinforced by NIR-II fluorescence imaging **(Figure 2d)**, which showed intense signals exclusively from nano-MBA and nano-MB upon 808 nm laser exposure.
Evaluation of thermal performance **(Figure 2g)** indicated that both nano-MB and nano-MBA achieved strong and closely matched photothermal responses, elevating the temperature of their dispersions to 55°C within 10 min under 808 nm laser irradiation at 0.8 W/cm². Quantitative analysis revealed photothermal conversion efficiencies of 28.54% for nano-MB and 33.13% for nano-MBA. These measurements confirm that the hybrid nano-MBA retains heat-generation performance equivalent to that of the enzyme-free nano-MB.

In vitro antibiofilm efficacy assessment
The therapeutic potential of nano-MBA against biofilm-associated infections was investigated using several complementary approaches, including crystal violet biofilm quantification, live/dead bacterial staining with confocal imaging, viable bacterial colony counting, and scanning electron microscopy for morphological analysis. As illustrated in **Figure 3a**, S. aureus (S.A.) biofilms exposed to NIR laser alone (PBS NIR+), blank nanovesicles (nano-RBM, both NIR+ and NIR−), or BPBBT-loaded nanovesicles without irradiation (nano-MB NIR−) showed no notable differences compared with the untreated control (PBS NIR−). These findings indicate that neither laser irradiation, empty nanovesicles, nor non-irradiated nano-MB alone affected biofilm integrity. In contrast, mono-PTT treatment with nano-MB under NIR irradiation resulted in a modest increase in biofilm biomass, suggesting

limited effectiveness of photothermal therapy alone against this particular S. aureus strain. Substantial biofilm reduction was achieved with nano-MA (both NIR+ and NIR−) and nano-MBA (both NIR+ and NIR−), demonstrating that α-amylase retained its biofilm-degrading capability even after encapsulation within RBC membrane nanovesicles. Most strikingly, nano-MBA combined with NIR-II laser irradiation degraded approximately 60% of the biofilm, while nano-MB under the same irradiation conditions led to a roughly 40% increase in biofilm mass **(Figure 3b)**. These data highlight the difficulty of eradicating this S. aureus biofilm using PTT monotherapy and underscore the substantial enhancement—approximately twofold—provided by the combined PTT and biofilm-degradation strategy.

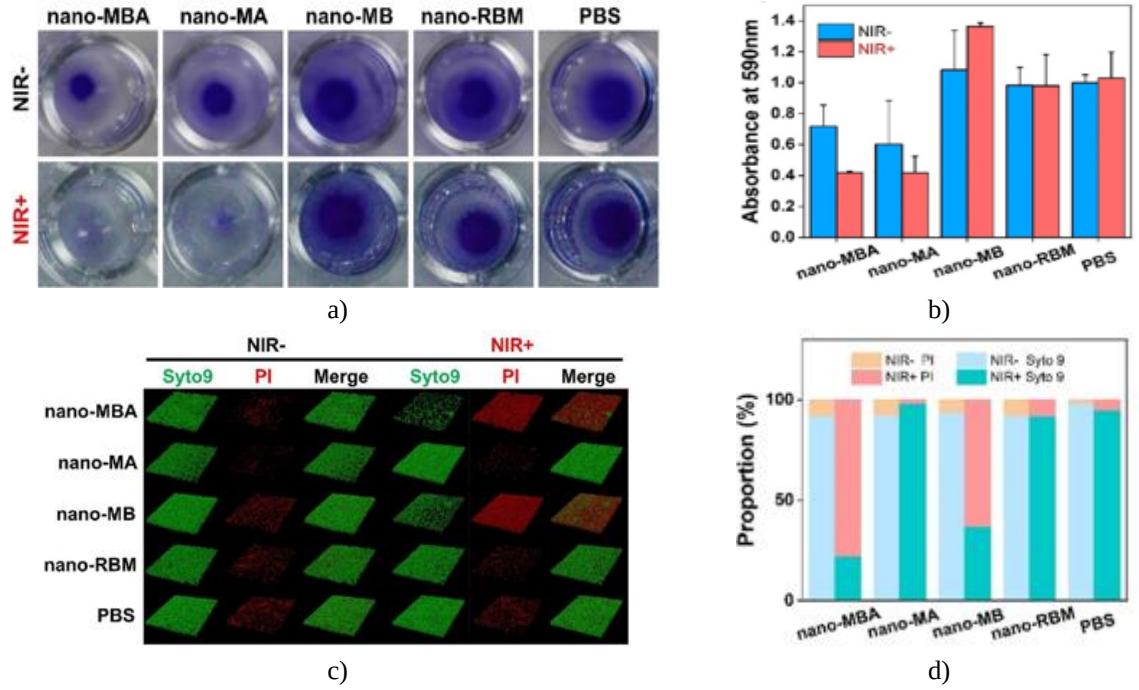

Figure 3. Quantification of S. aureus biofilms following various in vitro treatments. (a) Representative photographs of crystal violet-stained biofilms and (b) corresponding absorbance values measured at 590 nm after exposure to nano-MBA, nano-MA, nano-MB, nano-RBM, or PBS, with or without NIR laser irradiation (0.8 W/cm² at 808 nm for 10 min). (c) Three-dimensional confocal laser scanning microscopy (CLSM) images of S. aureus biofilms stained with SYTO 9 (live cells) and propidium iodide (PI, dead cells) after different treatments. (d) Quantitative ratio of live (SYTO 9) to dead (PI) bacterial fluorescence intensity in the treated biofilms.

Live/dead staining further assessed bacterial viability within the residual biofilm matrix. Confocal images **(Figure 3c)** revealed a pronounced increase in dead bacterial cells in groups treated with nano-MB (NIR+) and nano-MBA (NIR+) **(Figures 3c and 3d)**. No significant rise in dead cells was observed in biofilms treated with nano-MA (NIR+ or NIR−), nano-MB (NIR−), or nano-MBA (NIR−), consistent with the biofilm biomass quantification results **(Figures 3a and 3b)**. These observations indicate that α-amylase primarily disrupts the biofilm structure without direct bactericidal activity. Similarly, BPBBT-loaded nanovesicles (nano-MB and nano-MBA) lacked killing capacity in the absence of NIR irradiation. The potent bactericidal effect was therefore attributable to the photothermal action of BPBBT under laser exposure. The enzymatic degradation of the protective biofilm by α-amylase in nano-MBA (NIR+) rendered the embedded bacteria more vulnerable to thermal damage, yielding the strongest overall antibiofilm outcome. Consequently, the integration of enzymatic biofilm disruption with photothermal ablation markedly improves therapeutic efficacy against persistent biofilm infections.

Viable planktonic bacteria released from the biofilms were quantified using colony-counting assays. As shown in **Figures 4a**, treatment with nano-MB (NIR+) reduced viable planktonic bacteria by 36.1%, whereas nano-MBA (NIR+) achieved a 98.3% reduction, aligning closely with the live/dead imaging results. Scanning electron microscopy provided additional morphological evidence **(Figure 4b)**. Bacteria treated with PBS (NIR+), nano-RBM (NIR+ or NIR−), nano-MB (NIR−), or nano-MBA (NIR−) maintained intact cell membranes and normal

morphology, comparable to the untreated control (PBS NIR−). In contrast, exposure to nano-MB (NIR+) or nano-MBA (NIR+) caused severe membrane disruption and cellular damage. Collectively, these findings demonstrate that the synergistic combination of α-amylase-mediated biofilm degradation and BPBBT-based NIR photothermal therapy substantially augments antibacterial efficacy against biofilm-protected S. aureus infections.

In vivo NIR-II photothermal ablation of bacterial infections

Encouraged by the promising antibiofilm results obtained in vitro, the synergistic antibacterial performance of nano-MBA was further examined in an in vivo setting. Prior to efficacy studies, the retention and stability of nano-MBA at the infection site were evaluated. A severe subcutaneous abscess model was established by injecting 50 μL of a S. aureus (S.A.) suspension (10^9 CFU/mL) into the dorsal region of mice. Distinct abscess formation was evident 24 h post-inoculation. Subsequently, 50 μL of nano-MBA was locally administered into the abscess, followed by NIR-II fluorescence imaging and quantitative intensity analysis over 24 h. As presented in **Figure 5**, strong NIR-II fluorescence signals were observed at the abscess site immediately after injection **(Figure 5a)** and remained consistently stable throughout the 24 h observation period **(Figure 5b)**. This prolonged retention and photothermal stability support the potential for repeated treatments using nano-MBA. Ex vivo imaging of major organs confirmed that the nanovesicles did not disseminate systemically via the bloodstream and exhibited no accumulation in distant tissues **(Figures 5c and 5d)**. Moreover, both fluorescence and thermal imaging **(Figures 5a and 5c)** demonstrated uniform distribution of nano-MBA throughout the infected area, indicating its suitability for subsequent photothermal and combination therapies.

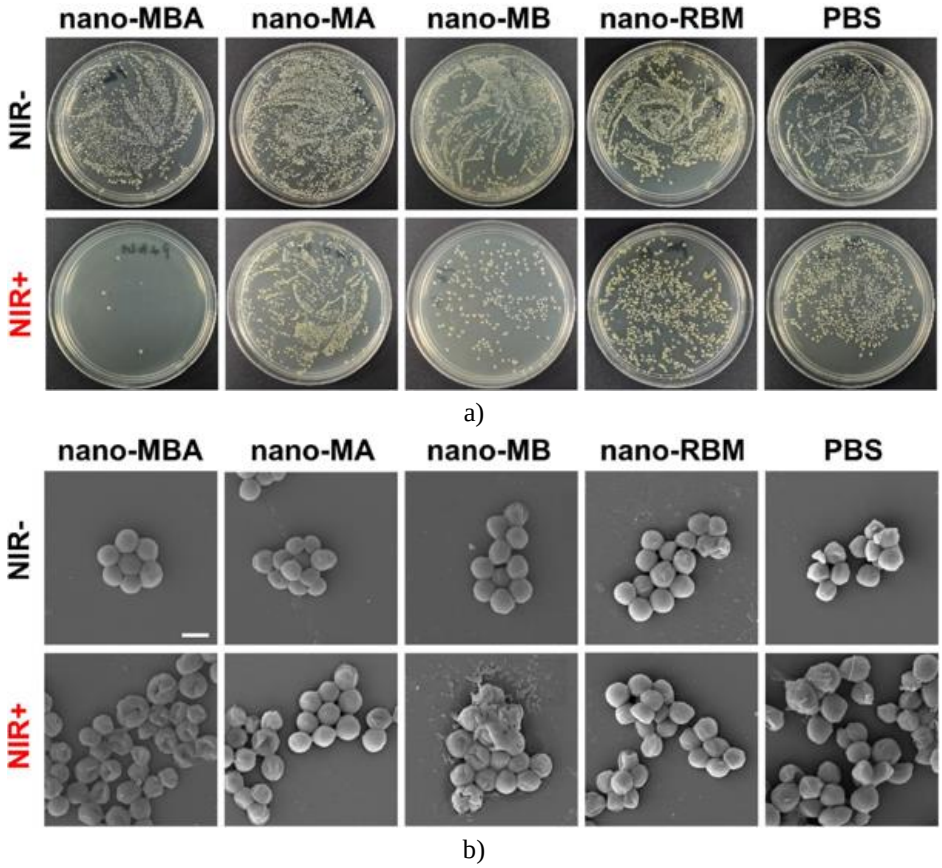

Figure 4. In vitro therapeutic efficacy of different treatment groups.
(a) Representative colony-forming unit images of viable planktonic bacteria recovered from each treatment.
(b) Scanning electron microscopy (SEM) images of S. aureus cells following various treatments. Scale bar: 1 μm.

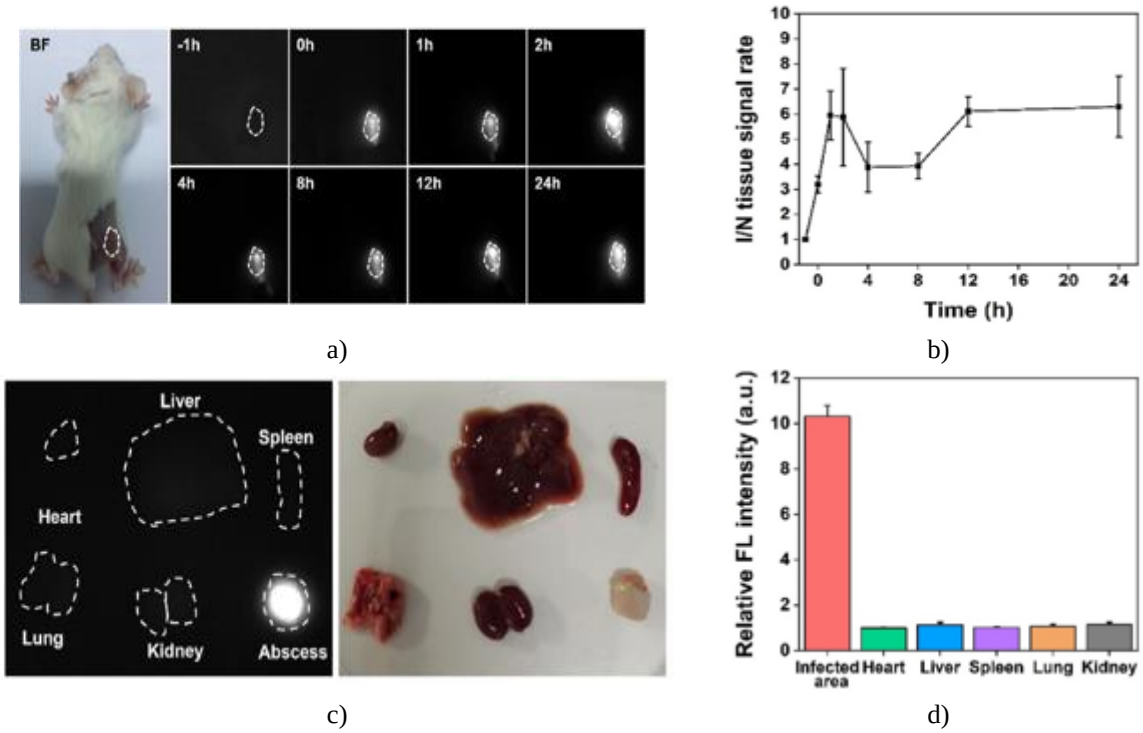

Figure 5. In vivo distribution and retention of nano-MBA.
(a) NIR-II fluorescence images of the infected site in S. aureus-infected mice following local injection of nano-MBA over a 24 h period. (b) Quantitative analysis of fluorescence intensity at the infection site as a function of time. (c) NIR-II fluorescence and bright-field images of major organs harvested 24 h after nano-MBA administration. (d) Biodistribution profile of nano-MBA in major organs 24 h post local administration. Error bars represent mean ± s.d. (n = 3).

For the therapeutic study, an additional 40 mice bearing subcutaneous abscesses were randomly allocated into eight treatment groups (n = 5 per group), balanced according to abscess size. The groups received nano-RBM (NIR+ and NIR−), nano-MA (NIR+ and NIR−), nano-MB (NIR+ and NIR−), or nano-MBA (NIR+ and NIR−). A safe laser power density of 0.8 W/cm² was applied, with continuous 808 nm laser irradiation for 8 min to implement photothermal or combination therapy. In groups containing BPBBT, the infected lesions reached a local temperature of approximately 50°C during irradiation.

Over the subsequent 6 days, abscess progression was monitored through photography **(Figure 6a)**, with abscess area and body weight recorded every other day **(Figures 6b and 6c)**. The nano-MBA (NIR+) group exhibited rapid and sustained abscess reduction after a single treatment, decreasing to less than 30% of the initial area by Day 6. In contrast, all other treatment groups showed only transient minor improvement on Day 3, followed by progressive abscess enlargement, reaching approximately 200% of the original size by Day 6. Due to the worsening condition observed in most groups, the experiment was concluded on Day 6. These in vivo results demonstrate that a single administration of the combined photothermal and enzymatic therapy using nano-MBA (NIR+) effectively resolved severe biofilm-associated infections, whereas monotherapy approaches failed to control disease progression.

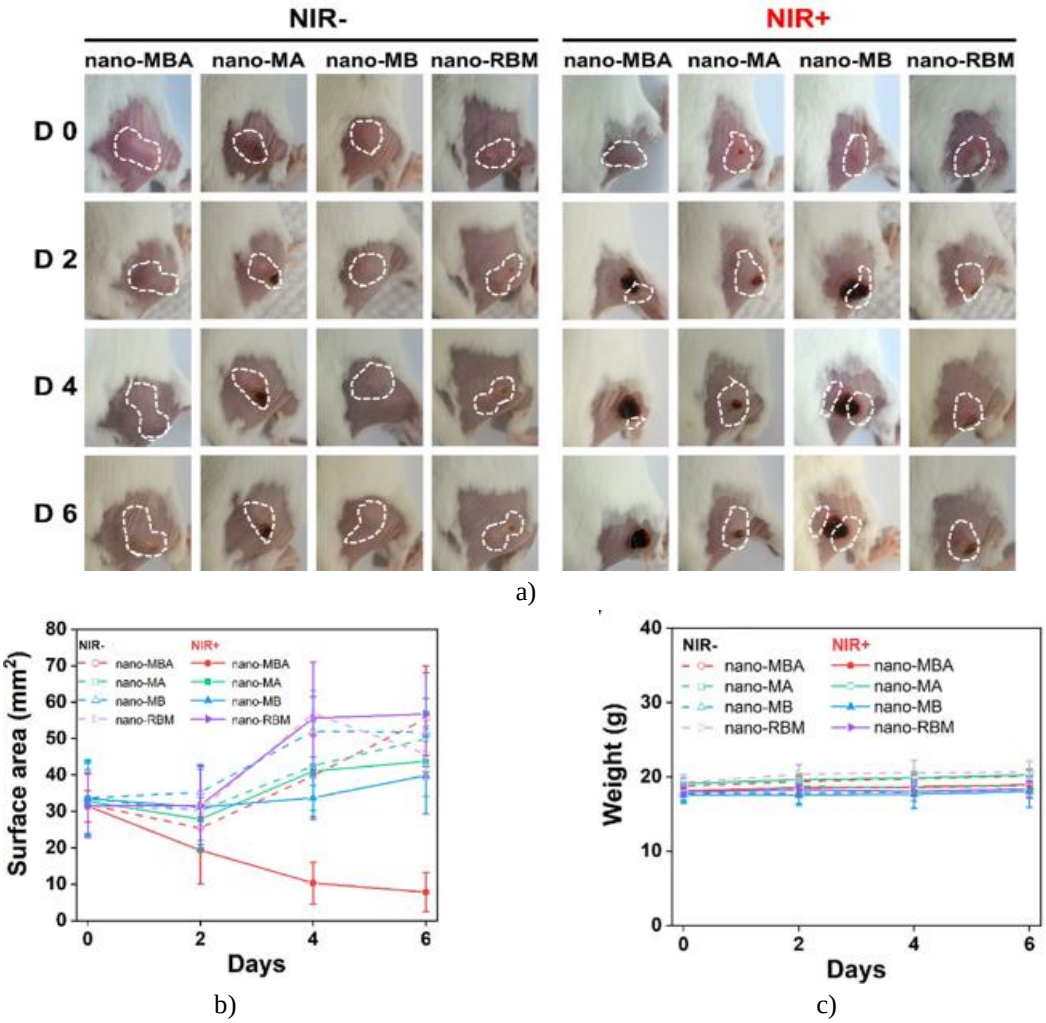

Figure 6. In vivo therapeutic efficacy of various formulations: nano-RBM (NIR+ and NIR−), nano-MA (NIR+ and NIR−), nano-MB (NIR+ and NIR−), and nano-MBA (NIR+ and NIR−). (a) Representative photographs of S. aureus biofilm-infected mice from each treatment group over a 6-day period following intervention. (b) Quantitative analysis of abscess area in each group at different time points. (c) Changes in body weight of mice throughout the treatment course. Error bars represent mean ± s.d. (n = 5). All NIR+ groups received 808 nm laser irradiation at 0.8 W/cm² for 10 min.

Following the completion of therapeutic monitoring, abscess tissues were harvested, homogenized, and analyzed to determine the number of viable bacteria remaining in the infected lesions. The nano-MBA (NIR+) treatment group exhibited a markedly lower bacterial burden compared with all other groups. Notably, although the S. aureus strain used in this biofilm infection model was not antibiotic-resistant and could not be readily distinguished from commensal bacteria typically present in murine skin and muscle, the combination therapy achieved superior bacterial clearance. Histological examination of subcutaneous inflammatory tissues **(Figure 7)** further demonstrated that both nano-MBA (NIR+) and nano-MB (NIR+) treatments substantially decreased inflammatory cell infiltration at the abscess sites, reflecting the antibacterial and anti-inflammatory properties of BPBBT within the developed nanoformulation [26]. In particular, the nano-MBA (NIR+) group displayed minimal to no inflammatory cell infiltration, confirming the superior therapeutic outcome of the combined enzymatic and photothermal approach.

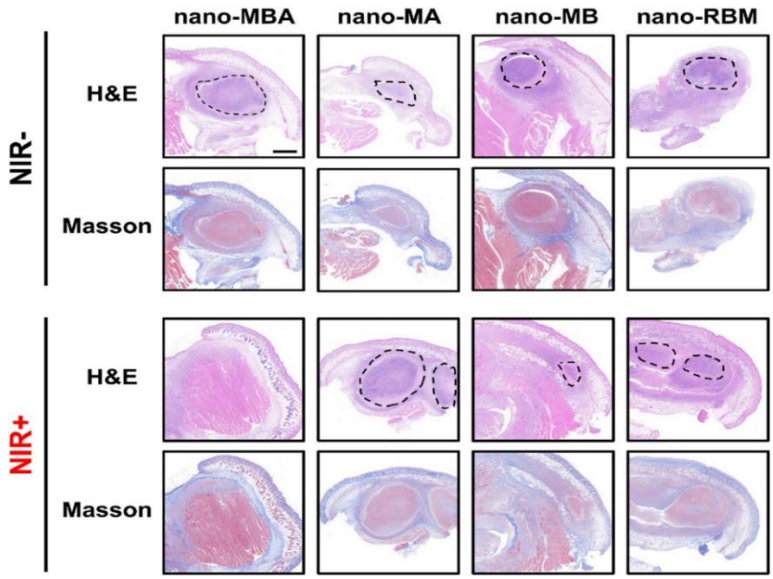

Figure 7. Histological evaluation using H&E and Masson's trichrome staining of infected tissues following different treatments. The regions enclosed by dotted boxes indicate areas of inflammatory cell infiltration. Scale bar: 1000 μm.

Biosafety evaluation

Incubation of 293T cells with varying concentrations of the different nanovesicles (nano-MBA, nano-MA, nano-MB, or nano-RBM; BPBBT concentrations of 20, 100, 150, 200, or 300 μg/mL) for 24 h in the dark resulted in negligible cytotoxicity, with cell viability remaining above 90% across all tested formulations. Hematological analysis revealed no significant alterations in blood parameters in healthy mice 24 h after administration of the nanovesicles, irrespective of 808 nm laser irradiation. In addition, liver and kidney function markers **(Figures 8a and 8b)** indicated the absence of acute hepatotoxicity or nephrotoxicity. Histological examination of major organs (heart, liver, spleen, lungs, and kidneys) after 6 days of treatment **(Figure 8c)** showed no observable structural damage or pathological changes. Overall, these findings confirm that the developed nanovesicles possess excellent biocompatibility, with no detrimental effects on normal cells, major organs, or induction of acute liver or kidney toxicity.

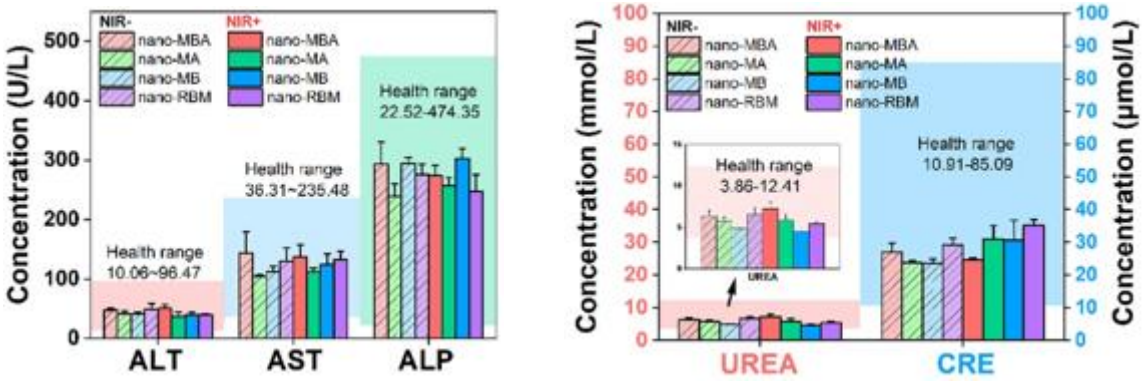

a) b)

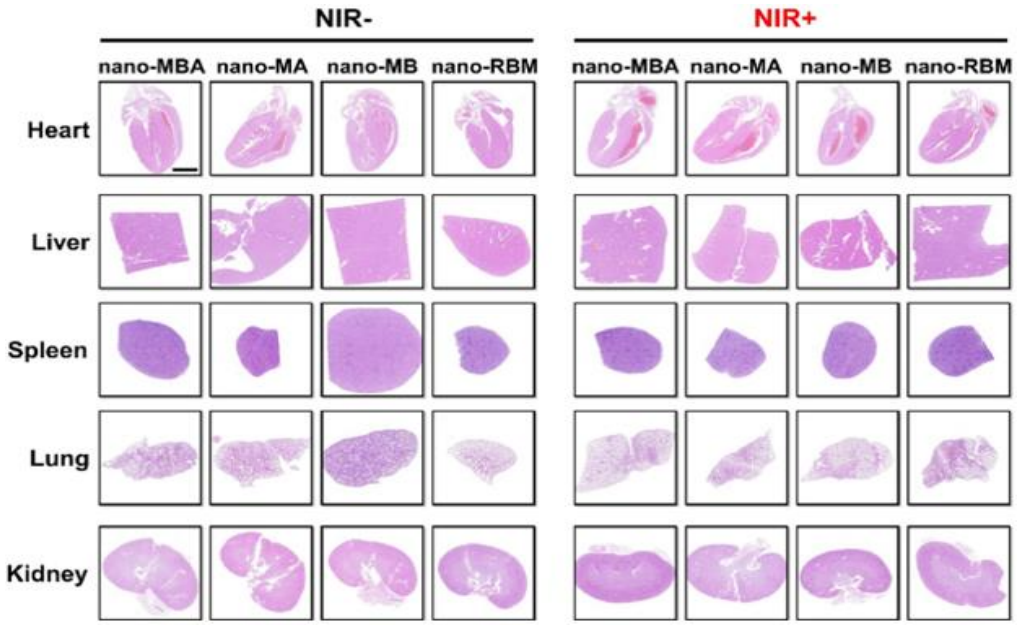

c)

Figure 8. In vivo biosafety verification.
(a) Serum levels of liver function biomarkers: alanine aminotransferase (ALT), aspartate aminotransferase (AST), and alkaline phosphatase (ALP). (b) Serum levels of kidney function biomarkers: urea (UREA) and creatinine (CRE). (c) H&E-stained images of major organs harvested after various treatments. Scale bar: 2000 μm. Error bars represent mean ± s.d. (n = 6). The NIR+ groups received 808 nm laser irradiation at 0.8 W/cm² for 10 min.

Conclusion

A novel biocompatible nanoformulation consisting of AIEgen-doped bioactive nanovesicles has been successfully engineered for mild-temperature photothermal antibiofilm therapy. This design enhanced the photothermal performance of BPBBT under 808 nm laser irradiation by restricting its intramolecular motions within the lipid bilayer of the RBC membrane. Application of nano-MBA enabled highly effective eradication of S. aureus biofilm infections at a safe temperature of 50°C in both in vitro and in vivo models. Relative to monotherapy approaches using either PTT alone or biofilm-degrading agents alone, the integrated strategy achieved markedly superior biofilm disruption and bactericidal activity. These outcomes underscore the value of combining NIR-II AIEgens with bioactive enzymes as a powerful approach for combating biofilm-associated infections, offering a compelling alternative to conventional antibiotic treatments. Comprehensive biosafety assessments further confirmed that the nanovesicles induced no detectable toxicity or adverse effects. Moreover, the co-encapsulation of AIEgens with other bioactive molecules within cell membrane-derived nanovesicles opens new avenues for the development of biomimetic platforms with broad therapeutic potential.

Acknowledgments: None

Conflict of Interest: None

Financial Support: None

Ethics Statement: None

References

1. Golan Y. Current treatment options for acute skin and skin-structure infections. Clin Infect Dis. 2019;68(Suppl 3):S206.

2. Shah M, Shah HD. Acute bacterial skin and skin structure infections: current perspective. Indian J Dermatol. 2011;56(5):510-4.
3. Bennett PM. Plasmid encoded antibiotic resistance: acquisition and transfer of antibiotic resistance genes in bacteria Br J Pharmacol. 2008;153(Suppl 1):S347-55.
4. Davies J, Davies D. Origins and evolution of antibiotic resistance. Microbiol Mol Biol Rev. 2010;74(3):417-33.
5. Lahiri D, Nag M, Banerjee R, Mukherjee D, Garai S, Sarkar T, et al. Amylases: biofilm inducer or biofilm inhibitor? Front Cell Infect Microbiol. 2021;11:660048.
6. Hall CW, Mah TF. Molecular mechanisms of biofilm-based antibiotic resistance and tolerance in pathogenic bacteria. FEMS Microbiol Rev. 2017;41(3):276-301.
7. Sharma S, Mohler J, Mahajan SD, Schwartz SA, Bruggemann L, Aalinkeel R. Microbial biofilm: a review on formation, infection, antibiotic resistance, control measures, and innovative treatment. Microorganisms. 2023;11(6):1614.
8. Hughes G, Webber MA. Novel approaches to the treatment of bacterial biofilm infections. Br J Pharmacol. 2017;174(14):2237-46.
9. Stewart PS, Costerton JW. Antibiotic resistance of bacteria in biofilms. Lancet. 2001;358(9276):135-8.
10. Al-Fawares O, Alshweiat A, Al-Khresieh RO, Alzarieni KZ, Rashaid AHB. A significant antibiofilm and antimicrobial activity of chitosan-polyacrylic acid nanoparticles against pathogenic bacteria. Saudi Pharm J. 2024;32(1):101918.
11. Liu X, Yang Y, Han M, Guo J, Liu H, Liu Y, et al. Guanylated hyperbranched polylysines with high in vitro and in vivo antifungal activity. Adv Healthc Mater. 2022;11(16):2201091.
12. Di Giulio M, Zappacosta R, Di Lodovico S, Di Campli E, Siani G, Fontana A, et al. Antimicrobial and antibiofilm efficacy of graphene oxide against chronic wound microorganisms. Antimicrob Agents Chemother. 2018;62(10):e01088-18.
13. He S, Jia X, Feng S, Hu J. Three strategies in engineering nanomedicines for tumor microenvironment-enabled phototherapy. Small. 2023;19(18):2300078.
14. Dubey T, Chinnathambi S. Photodynamic sensitizers modulate cytoskeleton structural dynamics in neuronal cells. Cytoskeleton (Hoboken). 2021;78(6):232-48.
15. Huang H, Ali A, Liu Y, Xie H, Ullah S, Roy S, et al. Advances in image-guided drug delivery for antibacterial therapy. Adv Drug Deliv Rev. 2023;192:114634.
16. Liu Y, Bhattarai P, Dai Z, Chen X. Photothermal therapy and photoacoustic imaging via nanotheranostics in fighting cancer. Chem Soc Rev. 2019;48(7):2053-108.
17. Xu J, Yao K, Xu Z. Nanomaterials with a photothermal effect for antibacterial activities: an overview. Nanoscale. 2019;11(18):8680-91.
18. Nguyen T, Duong HT, Selvanayagam R, Boyer C, Barraud N. Iron oxide nanoparticle-mediated hyperthermia stimulates dispersal in bacterial biofilms and enhances antibiotic efficacy. Sci Rep. 2015;5:18385.
19. Maleki A, He J, Bochani S, Nosrati V, Shahbazi M, Guo B. Multifunctional photoactive hydrogels for wound healing acceleration. ACS Nano. 2021;15(12):18895-917.
20. Chen X, Gao H, Deng Y, Jin Q, Ji J, Ding D. Supramolecular aggregation-induced emission nanodots with programmed tumor microenvironment responsiveness for image-guided orthotopic pancreatic cancer therapy. ACS Nano. 2020;14(5):5121-32.
21. Gu X, Kwok RT, Lam JW, Tang BZ. AIEgens for biological process monitoring and disease theranostics. Biomaterials. 2017;146:115-35.
22. Hong Y, Lam JW, Tang BZ. Aggregation-induced emission. Chem Soc Rev. 2011;40(11):5361-88.
23. Zhang R, Duan Y, Liu B. Recent advances of AIE dots in NIR imaging and phototherapy. Nanoscale. 2019;11(41):19241-50.
24. Zhao Z, Zhang H, Lam JW, Tang BZ. Aggregation-induced emission: new vistas at the aggregate level. Angew Chem Int Ed Engl. 2020;59(25):9888-907.
25. Zhang Z, Kang M, Tan H, Song N, Li M, Xiao P, et al. The fast-growing field of photo-driven theranostics based on aggregation-induced emission. Chem Soc Rev. 2022;51(6):1983-2030.
26. Huang Y, Li D, Wang D, Chen X, Ferreira L, Martins MCL, et al. A NIR-II emissive polymer AIEgen for imaging-guided photothermal elimination of bacterial infection. Biomaterials. 2022;286:121579.

27. Wang W, Gao Y, Zhang M, Li Y, Tang BZ. Neutrophil-like biomimic AIE nanoparticles with high-efficiency inflammatory cytokine targeting enable precise photothermal therapy and alleviation of inflammation. ACS Nano. 2023;17(8):7394-406.
28. Cui T, Wu S, Sun Y, Ren J, Qu X. Self-propelled active photothermal nanoswimmer for deep-layered elimination of biofilm in vivo. Nano Lett. 2020;20(10):7350-9.
29. Hu D, Zou L, Li B, Hu M, Ye W, Ji J. Photothermal killing of methicillin-resistant Staphylococcus aureus by bacteria-targeted polydopamine nanoparticles with nano-localized hyperpyrexia. ACS Biomater Sci Eng. 2019;5(10):5169-79.
30. Zhou Y, Zhou Z, Wu X, Wang Z, Qi W, Yang J, et al. Down-regulation of HSP by Pd-Cu nanozymes for NIR light triggered mild-temperature photothermal therapy against wound bacterial infection: in vitro and in vivo assessments. Int J Nanomedicine. 2023;18:4805-24.
31. Yuwen L, Xiao H, Lu P, Chen X, Li J, Xiu W, et al. Amylase degradation enhanced NIR photothermal therapy and fluorescence imaging of bacterial biofilm infections. Biomater Sci. 2023;11(1):63-75.
32. Huo J, Jia Q, Huang H, Zhang J, Li P, Dong X, et al. Emerging photothermal-derived multimodal synergistic therapy in combating bacterial infections. Chem Soc Rev. 2021;50(15):8762-89.
33. Mahdavi A, Sajedi R, Rassa M, Jafarian V. Characterization of an α-amylase with broad temperature activity from an acid-neutralizing Bacillus cereus strain. Iran J Biotechnol. 2010;8(2):103-10.
34. Alhamhoom Y, Kakinani G, Rahamathulla M, Osmani RAM, Hani U, Thajudeen KY, et al. Recent advances in the liposomal nanovesicles based immunotherapy in the treatment of cancer: a review. Saudi Pharm J. 2023;31(2):279-94.
35. Fernández-Borbolla A, García-Hevia L, Fanarraga ML. The role of microtubules in cancer progression and therapeutic resistance. Int J Mol Sci. 2024;25(4):2071.
36. Le Q, Lee J, Lee H, Shim G, Oh Y. The role of extracellular vesicles in cancer therapy. Acta Pharm Sin B. 2021;11(8):2096-112.
37. Xu C, Ju D, Zhang X. Exosomes in the tumor microenvironment: mechanisms and therapeutic applications. Front Immunol. 2022;13:923598.
38. Malhotra S, Dumoga S, Singh N. Recent advances in nanomedicine for cancer immunotherapy. Wiley Interdiscip Rev Nanomed Nanobiotechnol. 2022;14(3):e1776.
39. Qian G, Dai B, Luo M, Yu D, Zhan J, Zhang Z, et al. Band gap tuning of 1,4-bis(2-(4-(N,N-diphenylamino)phenyl)vinyl)benzene derivatives for efficient organic light-emitting diodes. Chem Mater. 2008;20(19):6208-14.
40. Gao S, Wei G, Zhang S, Zheng B, Xu J, Chen G, et al. Nanocatalytic tumour therapy by biomimetic metal-organic frameworks. Nat Commun. 2019;10(1):2206.
41. Yang X, Yang T, Liu Q, Zhang X, Yu X, Kwok RT, et al. AIEgen-based photodynamic therapy for bacterial infection. Adv Funct Mater. 2022;32(39):2206346.
42. Malachowa N, Kobayashi SD, Braughton KR, DeLeo FR. Mouse models of innate immunity. In: Allen IC, editor. Mouse Models of Innate Immunity. Totowa (NJ): Humana Press; 2013. p. 109-16. (Methods Mol Biol; vol. 1031).
43. Hu R, Lager E, Aguilar-Aguilar A, Liu J, Lam JW, Sung HH, et al. Twisted intramolecular charge transfer and aggregation-induced emission of 2-(2′-hydroxyphenyl)benzothiazole derivatives. J Phys Chem C. 2009;113(36):15845-53.
44. Yu Y, Xu Z, Zhao Z, Zhang H, Ma D, Lam JW, et al. Rational design of AIEgens with enhanced photosensitizing efficiency for photodynamic therapy. ACS Omega. 2018;3(11):16347-54.
45. Shi L, Liu Y, Li K, Sharma A, Yu K, Ji MS, et al. AIEgen-based photodynamic therapy for bacterial infection. Angew Chem Int Ed Engl. 2020;59(25):9962-70.
46. Zheng X, Wang D, Xu W, Cao S, Peng Q, Tang BZ. Aggregation-induced emission luminogens for effective photodynamic therapy. Mater Horiz. 2019;6(2):216-24.
47. Tan L, Li J, Liu X, Cui Z, Yang X, Zhu S, et al. Balancing the antibacterial activity and biocompatibility of metallic nanoparticles for biomedical applications. Adv Mater. 2018;30(35):1801808.
48. Yuan Z, Tao B, He Y, Liu J, Lin C, Shen X, et al. Biocompatible polydopamine nanoparticles for enhanced photothermal antibacterial therapy. Biomaterials. 2019;217:119290.